Cerebral Cortex, January 2017;27: 24–33

doi: 10.1093/cercor/bhw359
Advance Access Publication Date: 22 November 2016
Original Article

ORIGINAL ARTICLE

Deletion of Aquaporin-4 Curtails Extracellular Glutamate Elevation in Cortical Spreading Depression in Awake Mice

Rune Enger[1,2,†], Didrik B. Dukefoss[2,†], Wannan Tang[2], Klas H. Pettersen[2], Daniel M. Bjørnstad[2], P. Johannes Helm[2], Vidar Jensen[2], Rolf Sprengel[3,4], Koen Vervaeke[5], Ole P. Ottersen[6] and Erlend A. Nagelhus[1,2]

[1]Department of Neurology, Oslo University Hospital, N-0027 Oslo, Norway, [2]GliaLab and Letten Centre, Division of Physiology, Department of Molecular Medicine, Institute of Basic Medical Sciences, University of Oslo, N-0317 Oslo, Norway, [3]Department of Molecular Neurobiology, Max Planck Institute for Medical Research, D-69120 Heidelberg, Germany, [4]Max Planck Research Group at the Institute for Anatomy and Cell Biology, Heidelberg University, D-69120 Heidelberg, Germany, [5]Division of Physiology, Department of Molecular Medicine, Institute of Basic Medical Sciences, University of Oslo, N-0317 Oslo, Norway and [6]Division of Anatomy, Department of Molecular Medicine, Institute of Basic Medical Sciences, University of Oslo, N-0317 Oslo, Norway

Address correspondence to Rune Enger and Erlend A. Nagelhus, Department of Molecular Medicine, Institute of Basic Medical Sciences, University of Oslo, P.O. Box 1103 Blindern, N-0317 Oslo, Norway. Email: rune.enger@medisin.uio.no; e.a.nagelhus@medisin.uio.no

[†]These authors contributed equally to this work.

Abstract

Cortical spreading depression (CSD) is a phenomenon that challenges the homeostatic mechanisms on which normal brain function so critically depends. Analyzing the sequence of events in CSD holds the potential of providing new insight in the physiological processes underlying normal brain function as well as the pathophysiology of neurological conditions characterized by ionic dyshomeostasis. Here, we have studied the sequential progression of CSD in awake wild-type mice and in mice lacking aquaporin-4 (AQP4) or inositol 1,4,5-triphosphate type 2 receptor (IP3R2). By the use of a novel combination of genetically encoded sensors that a novel combination - an unprecedented temporal and spatial resolution, we show that CSD leads to brisk Ca^{2+} signals in astrocytes and that the duration of these Ca^{2+} signals is shortened in the absence of AQP4 but not in the absence of IP3R2. The decrease of the astrocytic, AQP4-dependent Ca^{2+} signals, coincides in time and space with a decrease in the duration of extracellular glutamate overflow but not with the initial peak of the glutamate release suggesting that in CSD, extracellular glutamate accumulation is extended through AQP4-dependent glutamate release from astrocytes. The present data point to a salient glial contribution to CSD and identify AQP4 as a new target for therapy.

Key words: AQP4, astrocyte, calcium, glia, homeostasis, IP3R2, migraine

Introduction

Cortical spreading depression (CSD) was discovered over 70 years ago (Leão 1944) and has intrigued neuroscientists ever since. This phenomenon—conserved through phylogeny from mudpuppy to man—represents a grave challenge to those homeostatic mechanisms that normally prevent inadvertent fluctuations of extracellular ion and glutamate concentrations in brain (Pietrobon and Moskowitz 2014; Ayata and Lauritzen 2015; Kramer et al. 2016). Studies of CSD not only increase our understanding of basic brain physiology but are also highly relevant for a number of neurological conditions including migraine and stroke (Charles and Baca 2013; Dreier and Reiffurth 2015; Seidel et al. 2016). In migraine, CSD is associated with the aura phase, while in stroke, CSD-like events are assumed to add to the damage caused by the ischemic event itself (ibid.).

Recent studies have shed new light on the sequence of events in CSD (Chuquet et al. 2007; Chang et al. 2010; Enger et al. 2015). Notably, at the CSD wavefront a prominent elevation of extracellular K^+ is followed by increases in neuronal Ca^{2+}, extracellular glutamate, and finally astrocytic Ca^{2+} (Enger et al. 2015). To assess whether the late phase of extracellular glutamate surge in CSD depends on astrocytic Ca^{2+} signals, we used 2 different gene knockout models: 1) *Aqp4*$^{-/-}$ mice, which show reduced astrocytic Ca^{2+} signaling during brain swelling (Thrane et al. 2011), and 2) *Itpr2*$^{-/-}$ mice, lacking the inositol 1,4,5-triphosphate type 2 receptor (IP3R2) that mediates Ca^{2+} release from the endoplasmic reticulum (Li et al. 2005).

So far, virtually all studies of CSD in live animals have been performed under anesthesia. The use of anesthesia may affect several of the processes that are inherent to CSD—including changes in extracellular space (ECS) volume (Xie et al. 2013)—and will thus limit the conclusions that can be made (Sonn and Mayevsky 2006). Ca^{2+} signaling in astrocytes is particularly sensitive to anesthesia (Thrane et al. 2012), implying that any involvement of glia should best be studied in awake animals.

Here, we used awake animals to provide strong evidence for a glial contribution to the extracellular glutamate overflow that occurs during CSD and is a hallmark of this condition. Using a novel combination of genetically encoded Ca^{2+} and glutamate sensors, we show that *Aqp4*$^{-/-}$ mice exhibit a shortening of CSD-induced Ca^{2+} signals in astrocytes, as well as a curtailed glutamate elevation in the ECS. Our findings suggest that in CSD, the late component of the extracellular glutamate overflow is of astrocytic origin and depends on the presence of AQP4 in astrocytes.

Materials and Methods

Animals

Male C57Bl/6N wild-type (WT) (Charles River Laboratories, Sulzfeld, Germany), *Aqp4*$^{-/-}$ (Thrane et al. 2011), and *Itpr2*$^{-/-}$ (Li et al. 2005) mice of at least 10 weeks of age were used for the experiments. Mice were housed on a 12 h light:12 h dark cycle (lights on at 8 AM), 1–4 mice per cage. All experimental groups contained at least 3 mice. Adequate measures were taken to minimize pain and discomfort. Experiments were carried out in accordance with the guidelines published in the European Communities Council Directive of November 24, 1986 (86/609/EEC). All procedures were approved by the Animal Use and Care Committee of the Institute of Basic Medical Sciences and the Faculty of Medicine at the University of Oslo.

Virus Production and Transfection

Serotype 2/1 recombinant adeno-associated virus (rAAV) from plasmid constructs pAAV-*GFAP*-GCaMP6f (Chen et al. 2013), pAAV-*GFAP*-iGluSnFR (Marvin et al. 2013), pAAV-*SYN*-jRGECO1a (Dana et al. 2016), and pAAV-*SYN*-jRCaMP1a (Dana et al. 2016) was generated as described (Tang et al. 2009), and purified by AVB Sepharose affinity chromatography (Smith et al. 2009) following titration with real-time PCR (rAAV titers about 1.0–6.0 × 10^{12} viral genomes {vg}/mL, TaqMan Assay, Applied Biosystems, Inc., Foster City, CA, USA). rAAV-*GFAP*-GCaMP6f and rAAV-*SYN*-jRGECO1a were mixed 1:1 and rAAV-*GFAP*-iGluSnFR and rAAV-*SYN*-jRCaMP1a were mixed 1:2. Approximately, 150 nL of the virus mixture were injected at each injection site.

Surgical Procedures and Induction of CSD

Anesthesia was induced in a chamber containing 3% isoflurane in room air enriched with 50% pure oxygen and subsequently maintained by nose cone flowing 1–1.5% isoflurane. Body temperature was kept at 37°C by a temperature-controlled heating pad. Buprenorphine 0.15 mg/kg was injected intraperitoneally, and the mice were left for 10 min before surgery started. The field was sterilized, and local anesthesia was accomplished by injection of bupivacaine (5 mg/mL).

The skull was exposed and cleaned. Groves were cut by scalpel in a checkboard pattern into the periosteum to enable strong adhesion of the cyanoacrylate glue that was subsequently applied concomitantly to the attachment of a custom-made titanium head bar. A 2.5-mm craniotomy with center coordinates anteroposterior 3.0 mm, lateral +2.5 mm relative to bregma was created as previously described (Takano et al. 2006). In short, a dental drill was used to carefully carve a circular groove in the skull with intermittent air puffs for the removal of debris until only approximately 0.1 mm of the bone thickness was left. The skull was then soaked for 10 min to soften before the bone flap was removed. Virus was injected at 3 sites, distributed to stay clear of vasculature and to infect the central parts of the exposed brain surface. A window made of 2 circular cover slips of 2.5 and 3.5 mm, respectively, glued together by ultraviolet curing glue (Huber et al. 2012) was then centered in the craniotomy, so that the glass plug very slightly depressed the dura. The window was subsequently fastened by dental cement.

Furthermore, a small secondary craniotomy was made approximately 4 mm rostral to the imaging window to allow epidural application of KCl (3 µL, 1M) for induction of CSD waves. This frontal craniotomy was temporarily covered by KWIK-SIL (World Precision Instruments, Sarasota, FL, USA). All exposed areas except the craniotomies were then covered with dental cement. Mice were treated with buprenorphin postoperatively for 2 days.

Additionally, in a subset of experiments, 2 silver wires (200 µm diameter, non-insulated) were implanted just above the dura through minimal craniotomies to enable recording of electrocorticograms (ECoG) during CSD. Care was taken to insulate the wires with glue and dental cement. Connectors for the wires were fastened onto the head bar.

To induce CSD, the KWIK-SIL plug in the rostral craniotomy was removed and a small droplet of KCl was added. KCl was only added once per day per animal, and usually the mice only displayed 1 CSD wave, but a subset of mice experienced several consecutive waves upon 1 KCl application. KWIK-SIL was reapplied after every trial. In a subset of experiments, strong

glial GCaMP6f fluorescence was present in the entire field of view when microscopy commenced. These Ca^{2+} signals likely represent startle-mediated responses activated by neuromodulatory pathways, as described by Srinivasan et al. (2015), rather than being a consequence of a CSD wave that had already passed. These videos were omitted from analyses.

Two-Photon Microscopy

Fluorescence was recorded by 2-photon laser scanning microscopy on a system assembled from components by Bruker/Prairie Technologies (Middleton, WI, USA) (model Ultima IV), Spectra Physics (Santa Clara, CA, USA) (laser model InSight DS), optical Table and opto mechanics by Standa Ltd. (Vilnius, Lithuania), optics by Bernhard Halle Nachfolger GmbH (Berlin, Germany), and electro optical modulators by Qioptiq/Gasenger (Gottingen, Germany). The microscope objective was a Nikon16 × 0.8 NA water-immersion objective (model CFI75 LWD 16XW; Tokyo, Japan).

All optical filters mentioned in the following description are by Chroma Technology Corporation (Bellows Falls, VT, USA). After having been reflected towards the detection unit by the main dichroic filter (type ZT473-488/594/NIRtpc), the signal light enters the system's 4-channel detector house, at the entrance of which a type ZET473-488/594/NIRm filter is installed, shielding the photomultiplier tubes from rest reflective light of the laser beams. Inside the detector house, the light is split into 2 fractions separated at 560 nm wavelength by the main signal light dichroic filter (T560lpxr). The "green" light (GCaMP6f and iGluSnFR fluorescence) is further guided by a secondary dichroic beam splitter at 495 nm (T495lpxr) and filtered by a ET525/50m-2p band-pass filter, whereas the "red" light (jRCaMP1a and jRGECO1a fluorescence) is similarly guided by a secondary beam splitter at 640 nm (T640lpxr) and subsequently filtered by a ET595/50m-2p band-pass filter. The photomultiplier tubes are Peltier cooled units, model 7422PA-40 by Hamamatsu Photonics K.K., Hamamatsu City, Japan.

Excitation wavelengths between 990 and 1020 nm were used. The first imaging session was performed at least 10 days after implantation of the chronic imaging window. Mice were then trained for 2–3 days with handling and getting used to head fixation on the spherical treadmill before data collection commenced. GCaMP6f (Chen et al. 2013), jRCaMP1a (Dana et al. 2016), jRGECO1a (Dana et al. 2016), or iGluSnFR (Marvin et al. 2013) fluorescence was captured in images of 300 × 300 pixels of approximately 170 × 170 μm areas in cortical layer 2/3 (120–200 μm below the pial surface) with frame rates of approximately 5 Hz. No obvious differences were noted between wavefront propagation in different depths.

Behavior and Electrophysiology

Acquisition of data was synchronized by custom-written LabVIEW software (National Instruments, Austin, TX, USA). Movements of the mice were recorded in 2 ways; namely by infrared-sensitive video surveillance and by tracking displacement of the treadmill. Movements of the treadmill were recorded by modified optical mice. Surveillance videos were analyzed in MATLAB (version R2015a; MathWorks, Inc., Natick, MA, USA) by quantifying mean absolute pixel difference per frame in between consecutive frames. This was done to also register movement that did not translate into ball motion (i.e., grooming and other forepaw movement). Thirty-second windows were manually placed to avoid signal artifacts, before (baseline) and during CSD, and subsequently mean values of mouse movement were calculated.

In a subset of experiments, ECoG traces were recorded (WT: 20 waves, 3 mice, *Aqp4*$^{-/-}$: 18 waves, 3 mice, *Itpr2*$^{-/-}$: 15 waves, 3 mice). We used a Multiclamp 700B amplifier with headstage CV-7B, and the signals were digitized by Digidata 1440 (both from Molecular Devices, LLC, Sunnyvale, CA, USA). ECoG data were analyzed by custom-written MATLAB scripts. To visualize the direct current (DC) shift accompanying CSD, the signals were low-pass filtered (0.5 Hz). To quantify the power in the respective frequency bands (delta: 1–5 Hz, theta: 6–9 Hz, alpha: 10–15 Hz, beta: 15–23 Hz, mu: 24–31 Hz), we first calculated the total power spectrum of 3-s intervals every 0.5 s by using the Welch method (Barlow 1985; Fenzl et al. 2007). The area under the curve for the respective frequency bands in the power spectra was then calculated. The same 3-second time windows as used for quantifying movement were used to calculate mean values of the power of the different bands.

Image Analysis

Imaging data were corrected for motion artifacts using the SIMA movement correction software (Kaifosh et al. 2014) and subsequently manually corrected if needed. Image segmentations and analyses were then performed with custom-written MATLAB scripts.

In double injected mice expressing GCaMP6f and jRGECO1a, regions of interests defining astrocytic compartments were carefully selected over somata, processes, and endfeet of cells with typical astrocyte morphology for the GCaMP6f signal. Similarly, neuronal somata and neuropil were segmented. The relative change in mean fluorescence (ΔF/F) over time was calculated for each region of interest and subsequently analyzed by custom-written MATLAB scripts. Baseline plus 2 SD was used as a threshold to identify fluorescent events.

For CSD velocity detection, we used a semiautomatic approach. We interactively drew the wavefront on a reference image, and a line perpendicular to the wavefront going through the center of the image was generated. We then performed an integrated pixel profile along this line (width 100 pixels) for all frames. The resultant average lines were plotted as xt plots, and the rise rate of the resultant wavefront was used to identify the wave propagation speed. These velocities were validated with manual measurements.

The time lags between the jRCaMP1a and iGluSnFR signal were too small to discern with our acquisition frame rate. However, in a single frame, the jRCaMP1a clearly increased ahead of the iGluSnFR signal. To quantify the distances between the 2 wavefronts, we performed an integrated pixel profile as described above (width 20 pixels) and assessed the distance between the wavefronts at 15% of maximum in the frames where the wavefronts were visible in both channels.

Statistics

Statistical analyses were performed using linear mixed effects models statistics in MATLAB. This method was chosen because of the hierarchical study design with observations grouped by experiment, mouse identity, and genotype, and that such models take into account the dependency between observations by including nested variance terms. Our model set genotype as the predictor variable and included random intercepts for mouse identity and experiment. All values are given as estimated

values by the mixed effects model with corresponding standard errors and P values.

Results

Two to six weeks following intracortical injection of virus with sensor construct, CSD was elicited in awake head-fixed mice through focal epidural application of KCl. The KCl was delivered through a small rostral craniotomy, and the CSD events were imaged through a chronic cranial window overlying the visual cortex (Fig. 1*a*). As reported by others, eliciting CSD was not associated with obvious discomfort (Koroleva and Bures 1993; Akcali et al. 2010). Typically, the mice stopped moving on the trackball during the DC shift and resumed their normal behavior within 1 min (Fig. 1*b* and Supplementary Movie 1). ECoG confirmed silencing of neuronal activity following the DC shift (Fig. 1*b*). The duration and amplitude of the DC shift did not differ between WT, *Aqp4*$^{-/-}$, and *Itpr2*$^{-/-}$ mice (Fig. 1*c*). Quantitative analysis of trackball movement, surveillance video, and ECoG confirmed that CSD was associated with reduced locomotion and mean power of all frequency bands (Fig. 1*d–f*).

The human synapsin (*SYN*) and glial fibrillary acidic protein (*GFAP*) promoters were used to target the red fluorescent Ca^{2+} sensor jRCaMP1a and the green fluorescent extracellular glutamate sensor iGluSnFR to neurons and astrocytes, respectively. Similar to our observations in anesthetized mice (Enger et al. 2015), CSD in awake mice was accompanied by brisk increases in neuronal Ca^{2+} and extracellular glutamate levels, traveling across the field of view as waves (Fig. 2*a* and Supplementary Movie 2). Both the amplitudes and the durations of the iGluSnFR fluorescence transients (Fig. 2*b*) were slightly reduced compared with what we reported previously in anesthetized mice (Enger et al. 2015).

We next assessed whether the extracellular glutamate elevation in CSD is dependent on astrocytic swelling and swelling-associated Ca^{2+} signals by using *Aqp4*$^{-/-}$ and *Itpr2*$^{-/-}$ mice (Supplementary Movies 3 and 4). In the former model, but not in the latter, the duration of the extracellular glutamate elevation was shortened by ~20 % (Table 1 and Fig. 2*b*; $P = 0.03$ for comparison of *Aqp4*$^{-/-}$ vs. WT and 0.46 for *Itpr2*$^{-/-}$ vs. WT). Deletion of the *Aqp4* gene did not alter the rise rate of the iGluSnFR fluorescent signal (Fig. 2*b*; WT: 6.4 ± 1.0 s, *Aqp4*$^{-/-}$: 6.3 ± 0.8 s, *n* as above, $P = 0.93$). However, the rise rate was significantly higher in *Itpr2*$^{-/-}$ mice than in WT mice (9.4 ± 1.0 s, *n* as above, $P = 0.03$ vs. WT and $P = 0.02$ vs. *Aqp4*$^{-/-}$). Both models displayed an increase in iGluSnFR peak amplitude (Table 1, Fig. 2*b*).

In anesthetized mice, we previously found that the CSD-associated increase in neuronal Ca^{2+} preceded the extracellular glutamate elevation by ~0.8 s (Enger et al. 2015). The time lag between the events was assessed by correlating the increase in GCaMP6f and iGluSnFR fluorescence—both green and thus expressed in separate animals—to the DC potential deflection. In this study, we combined sensors of different color—red jRCaMP1a and green iGluSnFR—and successfully measured the time lag between the Ca^{2+} signal and the glutamate wave in the same animal

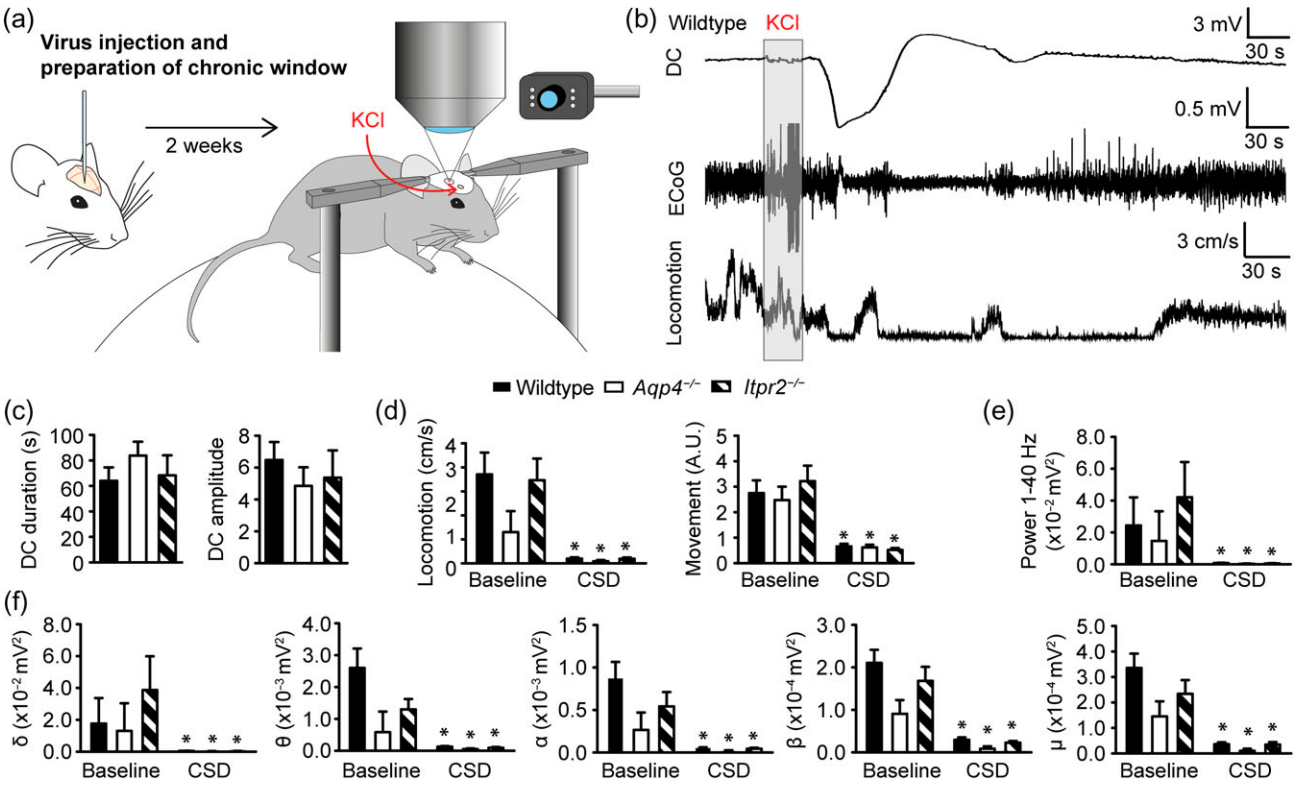

Figure 1. Experimental setup and animal monitoring. (*a*) Awake head-fixed mice positioned under the objective could move freely on a spherical treadmill. An infrared camera recorded animal behavior during the imaging session. CSD was triggered by KCl application through a small craniotomy rostral to the chronic cranial window. (*b*) Example traces illustrating the characteristic DC shift accompanying CSD waves, ECoG (band-pass filtered 1–40 Hz), and locomotion pattern during CSD. (*c*) Duration and amplitude of the DC shift. (*d*) Locomotion on the trackball and motion estimation from surveillance video before and during CSD. (*e* and *f*) Mean power before and during CSD for different frequency bands (cf. Materials and Methods for frequency ranges and numbers). *$P < 0.05$ for comparisons between baseline and during CSD.

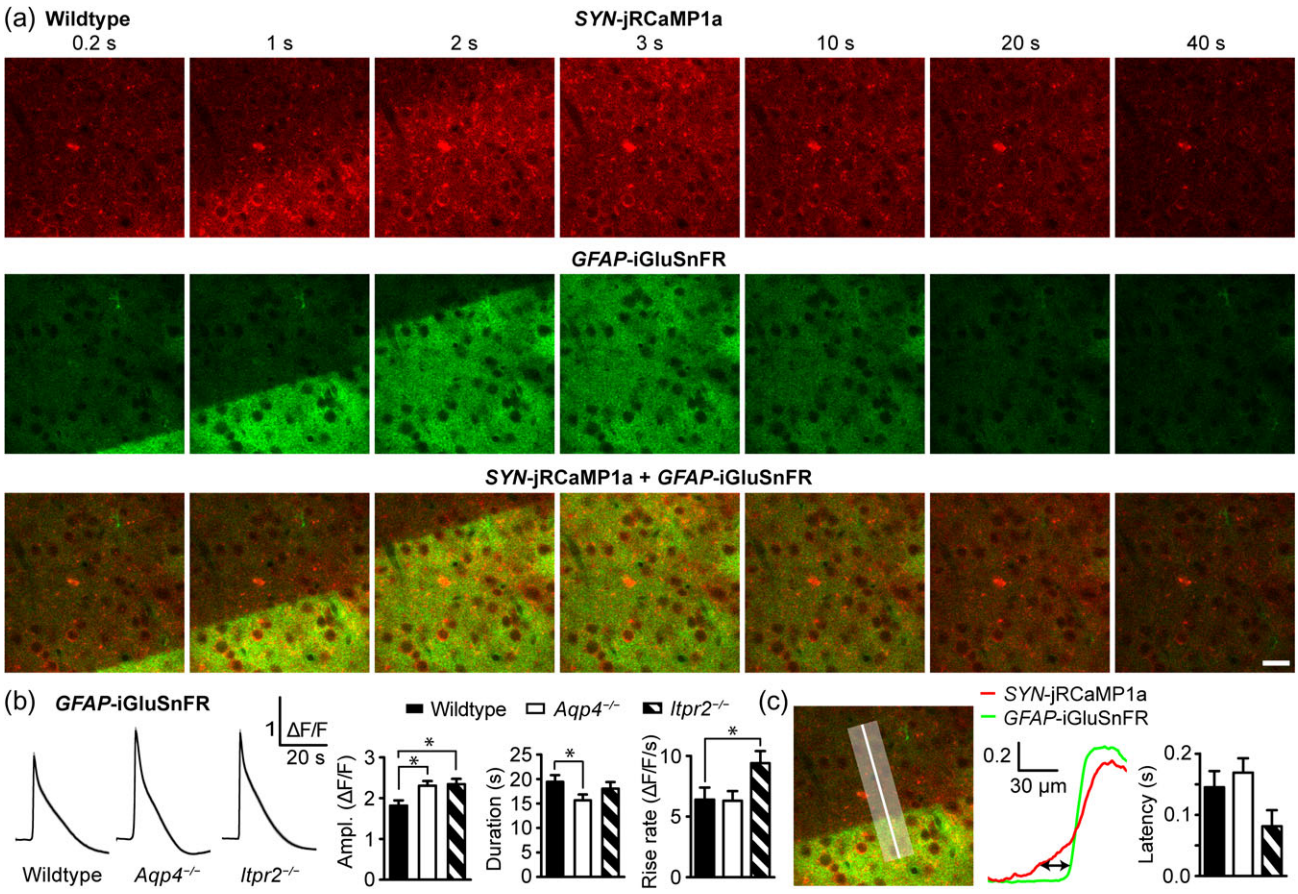

Figure 2. Dual color 2-photon imaging of neuronal Ca^{2+} signals and extracellular glutamate dynamics in the visual cortex of awake mice during CSD. (*a*) Time-lapse image series of neuronal $[Ca^{2+}]_i$ and extracellular glutamate dynamics as reported by jRCaMP1a (red) and iGluSnFR fluorescence (green), respectively, during passage of a CSD wave. (*b*) Average fluorescence traces, max amplitudes, and durations of iGluSnFR signals in CSD in WT, *Aqp4*$^{-/-}$ and *Itpr2*$^{-/-}$ mice. (*c*) Method for establishing time lag between $[Ca^{2+}]_i$ increases and rise in extracellular glutamate in CSD. Arrows indicate the points of each curve in between which the distances were measured. An integrated linescan was performed normal to the CSD wavefront. The distance between the neuronal Ca^{2+} wavefront and the glutamate wavefront (defined as 15% of max fluorescence) was determined for all frames where the wavefronts were visible in the field of view, and these distances were converted to a corresponding time lag based on the velocity of the individual CSD wave. Scale bars indicate relative fluorescence increase along the linescan. Mean time lags between neuronal $[Ca^{2+}]_i$ increase and glutamate increase. Scale bars: 25 μm. *$P < 0.05$; error bars, SE.

(Fig. 2*c*). Although the neuronal Ca^{2+} increase preceded the extracellular glutamate elevation in both anesthetized and awake animals, the lag between the 2 events was much shorter in awake animals. However, the lag did not differ significantly between WT, *Aqp4*$^{-/-}$, and *Itpr2*$^{-/-}$ mice (WT: 0.15 ± 0.03 s, $n = 199$ measurements, 19 waves, 4 mice; *Aqp4*$^{-/-}$ mice: 0.17 ± 0.02 s, $n = 256$ measurements, 22 waves, 4 mice; *Itpr2*$^{-/-}$ mice: 0.08 ± 0.03 s, $n = 200$ measurements, 17 waves, 4 mice; $P = 0.50$ and 0.16 for WT vs. *Aqp4*$^{-/-}$ and *Itpr2*$^{-/-}$, respectively) (Fig. 2*c*, right).

To characterize the effects of *Aqp4* and *Itpr2* gene deletion on neuronal and astrocytic Ca^{2+} signals, we performed dual color imaging with jRGECO1a—an optimized red-shifted Ca^{2+} sensor that exhibits higher response amplitude and faster decay kinetics than jRCaMP1a (Dana et al. 2016)—and GCaMP6f (Fig. 3*a* and Supplementary Movies 5–7). Again, the human *SYN* and *GFAP* promoters were used to target sensor to neurons and astrocytes, respectively.

In neurons and their processes, the amplitude and duration of the CSD-associated Ca^{2+} transients did not differ between *Aqp4*$^{-/-}$ and WT mice. Neither did *Itpr2* knockout alter the neuronal Ca^{2+} transients, except for modestly reducing the amplitude (Table 1 and Fig. 3*b*,*c*; peak ΔF/F, neuronal somata: $P = 0.56$ for *Aqp4*$^{-/-}$ vs. WT and 0.009 for *Itpr2*$^{-/-}$ vs. WT; peak ΔF/F, neuronal processes: $P = 0.34$ for *Aqp4*$^{-/-}$ vs. WT and 0.01 for *Itpr2*$^{-/-}$ vs. WT; duration, neuronal somata: $P = 0.29$ for *Aqp4*$^{-/-}$ vs. WT and 0.60 for *Itpr2*$^{-/-}$ vs. WT; duration, neuronal processes: $P = 0.08$ for *Aqp4*$^{-/-}$ vs. WT and 0.12 for *Itpr2*$^{-/-}$ vs. WT).

In contrast, the astrocytic Ca^{2+} dynamics differed strikingly between the 3 genotypes (Fig. 3*b*,*c*). The amplitude of the Ca^{2+} transients in astrocytic somata, processes, and endfeet was unaffected by *Aqp4* deletion but severely attenuated in the absence of IP3R2 (Table 1 and Fig. 3*c*; peak ΔF/F, astrocytic somata: $P = 0.75$ for *Aqp4*$^{-/-}$ vs. WT and <0.001 for *Itpr2*$^{-/-}$ vs. WT; peak ΔF/F, astrocytic processes, $P = 0.49$ for *Aqp4*$^{-/-}$ vs. WT and <0.001 for *Itpr2*$^{-/-}$ vs. WT; peak ΔF/F, astrocytic endfeet, $P = 0.56$ for *Aqp4*$^{-/-}$ vs. WT and <0.001 for *Itpr2*$^{-/-}$ vs. WT). In contrast, the duration of the astrocytic Ca^{2+} transients was shortened in all astrocytic compartments in *Aqp4*$^{-/-}$ and prolonged in *Itpr2*$^{-/-}$ mice (Table 1 and Fig. 3*c*; astrocytic somata, $P < 0.001$ for both *Aqp4*$^{-/-}$ and *Itpr2*$^{-/-}$ mice vs. WT; astrocytic processes, $P = 0.008$ for *Aqp4*$^{-/-}$ vs. WT and <0.001 for *Itpr2*$^{-/-}$ vs. WT; astrocytic endfeet, $P = 0.02$ for *Aqp4*$^{-/-}$ vs. WT and 0.01 for *Itpr2*$^{-/-}$ vs. WT).

The CSD-associated Ca^{2+} transients in awake WT mice started 1.3 ± 0.1 s ($n = 36$ cell pairs, 12 waves, 4 mice) later in

Table 1 Changes in the levels of extracellular glutamate, neuronal Ca^{2+}, and astrocytic Ca^{2+} in CSD

	WT	*Aqp4*$^{-/-}$	*Itpr2*$^{-/-}$
GFAP-iGluSnFR			
Max ΔF/F	1.8 ± 0.1	2.3 ± 0.1	2.3 ± 0.1
Duration (s)	19.5 ± 1.3	15.7 ± 1.2	18.1 ± 1.3
n (ROIs, waves, mice)	279, 19, 4	340, 22, 4	273, 17, 3
SYN-jRGECO1a			
Neuronal somata			
Max ΔF/F	4.0 ± 0.2	3.8 ± 0.2	3.1 ± 0.3
Duration (s)	46.6 ± 2.9	42.1 ± 3.1	44.0 ± 3.9
n (ROIs, waves, mice)	145, 22, 4	133, 19, 4	94, 12, 4
Neuronal processes			
Max ΔF/F	4.6 ± 0.2	4.3 ± 0.3	3.7 ± 0.3
Duration (s)	43.1 ± 2.5	36.1 ± 2.6	42.6 ± 3.3
n (ROIs, waves, mice)	299, 28, 4	296, 24, 4	191, 18, 3
GFAP-GCaMP6f			
Astrocyte somata			
Max ΔF/F	4.6 ± 0.5	4.3 ± 0.5	1.7 ± 0.5
Duration (s)	20.7 ± 1.6	11.3 ± 1.8	30.1 ± 2.7
n (ROIs, waves, mice)	62, 19, 4	59, 19, 4	58, 14, 3
Astrocyte processes			
Max ΔF/F	3.8 ± 0.5	4.4 ± 0.6	1.5 ± 0.6
Duration (s)	15.6 ± 1.4	10.0 ± 2.6	26.0 ± 1.5
n (ROIs, waves, mice)	79, 28, 4	60, 28, 4	74, 19, 3
Astrocyte endfeet			
Max ΔF/F	5.3 ± 0.7	4.7 ± 0.7	1.7 ± 0.2
Duration (s)	19.4 ± 1.5	14.3 ± 1.6	25.0 ± 1.6
n (ROIs, waves, mice)	46, 24, 4	34, 20, 4	41, 19, 3

astrocytes than in neurons (Fig. 3*d*), a lag much shorter than previously reported for anesthetized mice (~3 s, cf. Enger et al. 2015). This time lag did not differ between *Aqp4*$^{-/-}$, *Itpr2*$^{-/-}$, and WT mice (Fig. 3*d*; *Aqp4*$^{-/-}$: 1.2 ± 0.1 s, $n = 31$ cell pairs, 12 waves, 4 mice; *Itpr2*$^{-/-}$: 1.8 ± 0.2 s, $n = 81$ cell pairs, 18 waves, 3 mice; $P = 0.97$ and 0.20 for *Aqp4*$^{-/-}$ and *Itpr2*$^{-/-}$ vs. WT, respectively).

The CSD wave propagation speed in WT mice was 4.6 ± 0.2 mm/min ($n = 27$ waves, 4 mice; Fig. 3*e*), that is, ~50% faster than reported for anesthetized mice (Enger et al. 2015). In contrast to the findings of Yao et al. (2008), we found no difference in wave propagation speed between *Aqp4*$^{-/-}$ (4.6 ± 0.2 mm/min, $n = 24$ waves, 4 mice) and WT mice ($P = 0.81$). The speed was increased by ~20% in *Itpr2*$^{-/-}$ vs. WT mice (5.4 ± 0.2 mm/min, $n = 18$ waves, 3 mice, $P = 0.002$ for *Itpr2*$^{-/-}$ vs. WT).

Discussion

Induction of CSD is mobilizing a series of events that challenge the mechanisms that are normally responsible for the brain's ion and glutamate homeostasis (Pietrobon and Moskowitz 2014; Ayata and Lauritzen 2015; Kramer et al. 2016). Thus, CSD offers a window through which one may achieve a detailed understanding of both basic brain functions and the multiple neurological conditions in which essential homeostatic mechanisms are compromised.

Great strides have been made in studies that have employed specific sensors for those ions and transmitters that are perturbed in CSD. Our previous study in anesthetized mice revealed a stereotypical sequence of events, starting with an extracellular K^+ increase that in turn causes neurons to depolarize and to release glutamate into the ECS (Enger et al. 2015). We found that the CSD wave is associated with brisk neuronal Ca^{2+} signaling that precedes the glutamate release.

However, the complex mechanisms underlying CSD are best studied in awake animals since anesthetics are known to bind to and allosterically modulate a number of receptors that might be involved in the propagation of CSD (Orser et al. 2002). Thus, depending on the type of agent used, anesthesia will affect such diverse factors as susceptibility to CSD (Kudo et al. 2008), basal K^+ levels (Sonn and Mayevsky 2006), neuronal excitability (Orser et al. 2002), gap junctional coupling (Liu et al. 2016), glial Ca^{2+} signaling (Thrane et al. 2012), ECS volume (Xie et al. 2013), and vascular dynamics (Tran and Gordon 2015). In agreement, here we found that the speed by which the CSD wavefronts move in awake animals exceeds by 50% the corresponding speed in anesthetized animals. Furthermore, the time lag between onset of neuronal Ca^{2+} signals and onset of glial Ca^{2+} signals is shorter in awake than in anesthetized mice (1 vs. 3 s), as is the delay between the appearance of neuronal Ca^{2+} signals and elevation of extracellular glutamate (0.1 vs. 0.8 s).

A major outstanding question—and the focus of this study—relates to the involvement of astrocytes in CSD. Studies from several laboratories indicate that CSD elicits Ca^{2+} signals in astrocytes (Basarsky et al. 1998; Peters et al. 2003; Lian and Stringer 2004), and that these signals are delayed compared with the neuronal Ca^{2+} signals (Chuquet et al. 2007; Enger et al. 2015). Here, we used a novel combination of sensors in WT and gene knockout mice to simultaneously analyze cellular Ca^{2+} signals and extracellular glutamate concentrations in awake animals during CSD. This innovative approach allowed us to conclude that astrocytes regulate the duration of the extracellular glutamate increase in CSD, and that this regulation depends on the presence of the water channel AQP4. Pertinent to CSD, AQP4 has been implicated in a number of homeostatic processes, beyond its primary role as a water transporter (Nagelhus and Ottersen 2013; Verkman et al. 2014). A range of studies has pointed to an involvement of AQP4 in volume and K^+ homeostasis (Amiry-Moghaddam et al. 2003a, 2003b; Padmawar et al. 2005; Binder et al. 2006; Yao et al. 2008; Haj-Yasein et al. 2011, 2012; Thrane et al. 2013; Haj-Yasein et al. 2015). Furthermore, in a model of acute edema, the frequency of glial Ca^{2+} signaling was found to be significantly reduced in *Aqp4*$^{-/-}$ mice (Thrane et al. 2011).

Two important observations were made in this study. First, depletion of AQP4 reduces the duration of CSD-induced astrocytic Ca^{2+} signals. Second, depletion of AQP4 reduces the duration of the glutamate overflow in the ECS. Therefore, we hypothesize that the late phase or "tail" of glutamate release in CSD is secondary to astrocytic Ca^{2+} signaling and is not due to ongoing neuronal activity. Our findings that the Ca^{2+} signals in glial processes always fade out a few seconds prior to normalization of the extracellular glutamate level in CSD (cf. Fig. 3*c* with Fig. 2*b*) are in agreement with the idea that glial Ca^{2+} signaling is upstream of—and not downstream of—the extracellular glutamate overflow in the late phase of CSD. Our finding that CSD-induced astrocytic Ca^{2+} signals depend on AQP4 suggests that astrocytes swell during CSD, likely due to K^+ uptake. It is well documented that extracellular K^+ elevation induces swelling of glia (MacAulay and Zeuthen 2012).

The amplitude and duration of neuronal Ca^{2+} signaling was unchanged after *Aqp4* deletion. This was expected as neurons do not express AQP4. Hence, there is no evidence of a neuronal contribution to the changes observed in duration of extracellular glutamate overflow.

As an additional attempt to establish a causal link between glial Ca^{2+} signaling and the observed shortening of the extracellular glutamate elevation, we induced CSD in animals with targeted deletion of *Itpr2* (Li et al. 2005). We expected that the

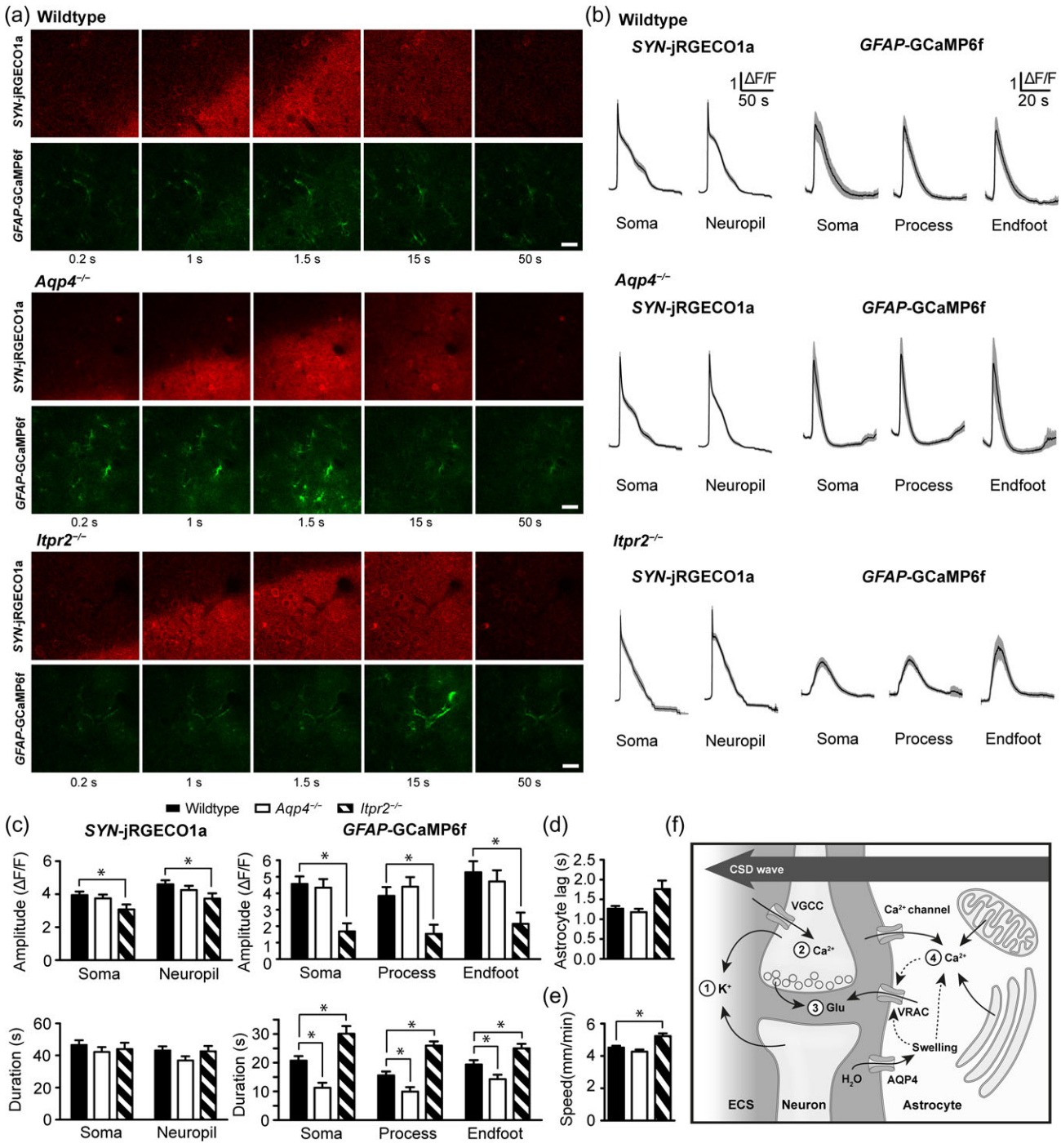

Figure 3. Simultaneous monitoring of neuronal and astrocytic Ca^{2+} levels in CSD. (*a*) Time-lapse image series of the neuronal jRGECO1a (red) and astrocytic GCaMP6f fluorescence (green) during passage of a CSD wave in WT, *Aqp4*$^{-/-}$ and *Itpr2*$^{-/-}$ mice. Merged snapshot images are shown to the right. (*b*) Average fluorescence traces of neuronal jRGECO1a signals and astrocytic GCaMP6f signals in the 3 different genotypes. (*c*) Max amplitudes and durations of the fluorescent responses in astrocytic and neuronal compartments in the 3 genotypes. (*d*) Time lag between the astrocytic and neuronal Ca^{2+} increase. (*e*) CSD wave propagation speed in the 3 genotypes. (*f*) Cartoon showing sequence of events in CSD, including the proposed mechanism by which AQP4 modulates extracellular glutamate levels in the late phase of CSD. A K^+ surge in the ECS causes neuronal depolarization and activation of voltage-gated Ca^{2+} channels (VGCC), leading to Ca^{2+}-dependent vesicular release of glutamate. AQP4 facilitates astrocytic water uptake in face of high extracellular potassium. The resultant swelling triggers intracellular Ca^{2+} signaling and glutamate release (dashed arrows) through Ca^{2+}-sensitive volume regulatory anion channels (VRAC). Scale bars: 25 μm. *$P < 0.05$; error bars, SE.

removal of this receptor would abolish the astrocytic Ca^{2+} signals and hence eliminate the tail of the CSD-induced extracellular glutamate increase. To our surprise, we found that the *Itpr2*$^{-/-}$ mice showed marked astrocytic Ca^{2+} signals, albeit with a lower amplitude and lacking the fast component. Importantly, the Ca^{2+} signals in the *Itpr2*$^{-/-}$ mice were not shortened. Neither was a shortening observed of the extracellular glutamate elevation, in line with what one would expect if the glutamate elevation reflects the duration of the astrocytic Ca^{2+} signals. Thus, we conclude that Ca^{2+} release from the

endoplasmic reticulum of astrocytes, which is IP3R2 dependent, is not required for the astrocytic glutamate release that occurs in the late phase of CSD. Alternative sources of Ca^{2+} include mitochondria and transient receptor potential (TRP) channels in the plasma membrane (Shigetomi et al. 2016). TRP channels are stretch-sensitive and might be activated through AQP4-mediated cell swelling. The attenuated glutamate overflow observed in the absence of AQP4 cannot be attributed to changes in the ECS volume, as the rise rate for glutamate is the same in *Aqp4*$^{-/-}$ and WT mice (Fig. 2*b*). Nor can this effect be explained by an upregulation of glutamate uptake. Thus, studies show that depletion of AQP4 leads to a downregulation rather than an upregulation of the glial glutamate transporter 1 (Li et al. 2012) without affecting the expression of Kir4.1 potassium channels (Zhang and Verkman 2008; Haj-Yasein et al. 2015), which indirectly regulate uptake (Djukic et al. 2007). Furthermore, knock out of the *Aqp4* gene does not affect blood–brain barrier integrity (Saadoun et al. 2009; Eilert-Olsen et al. 2012) or blood flow dynamics in CSD (Thrane et al. 2013). It deserves emphasis that AQP4 and Ca^{2+}-dependent glutamate release from glia need not be vesicular in nature. Thus, volume regulated anion channels and other membrane channels might release glutamate and other excitatory amino acids in a Ca^{2+}-dependent fashion (Malarkey et al. 2008; Minieri et al. 2015; Mongin 2016).

Conclusion

Our data indicate that in CSD, the late phase of glutamate overflow is determined by the duration of astrocytic Ca^{2+} signals. Specifically, we assume that the elevation of extracellular glutamate—initially brought about by neuronal activity—is prolonged through glia-mediated glutamate release, and that this glial glutamate release is triggered by AQP4-dependent swelling evoked by the extracellular K^+ increase. Our findings point to an important glial contribution to extracellular glutamate in CSD (Fig. 3*f*). This would be in line with our previous data showing that targeted AQP4 removal affords protection in an experimental stroke model (Amiry-Moghaddam et al. 2003a).

The approach used here allows for an unprecedented spatial and temporal resolution. In previous studies, with only 1 fluorophore available, Ca^{2+} signaling and glutamate elevation could not be studied in the same animals. Thus, correlative analyses were required (Enger et al. 2015). Here, we employ a new fluorophore that allows the 2 parameters to be analyzed in the same animal and within the same region of interest. Our experimental design also permitted us to avoid the confounding effects of using an acute window preparation. Acute windows with disruption of the dura inevitably lead to cortical herniation that may interfere with the processes being studied.

The technology that now opens for optical imaging of complex mechanistic processes in awake animals provides a platform for more detailed studies—the potential of which will be limited largely by the availability of specific sensors. We envisage a future where the indicators used here can be accompanied by sensors for Na^+, K^+, H^+, GABA, and several other ions and molecules so as to arrive at an even better understanding of the sequence of events that constitutes the signature of CSD. Through such studies, it will eventually be possible to identify novel targets for effective treatment of CSD in the waking state.

Supplementary Material

Supplementary material can be found at: http://www.cercor.oxfordjournals.org/.

Funding

South-Eastern Norway Regional Health Authority (grant #2013021 to E. A. N.); the Research Council of Norway (grants #226696 and #240476 to E. A. N. and #231495 to K. V.); the European Union's Seventh Framework Programme for research, technological development, and demonstration under grant agreement no. 601055; the European Research Council (grant #639272 to K. V.); German Research Council (grant SFB1134/B01 to R. S.); the Molecular Life Science Initiative at the University of Oslo and the Letten Foundation.

Notes

Conflict of Interest: None declared.

References

Akcali D, Sayin A, Sara Y, Bolay H. 2010. Does single cortical spreading depression elicit pain behaviour in freely moving rats? Cephalalgia. 30:1195–1206.

Amiry-Moghaddam M, Otsuka T, Hurn PD, Traystman RJ, Haug FM, Froehner SC, Adams ME, Neely JD, Agre P, Ottersen OP, et al. 2003a. An alpha-syntrophin-dependent pool of AQP4 in astroglial end-feet confers bidirectional water flow between blood and brain. Proc Natl Acad Sci USA. 100:2106–2111.

Amiry-Moghaddam M, Williamson A, Palomba M, Eid T, de Lanerolle NC, Nagelhus EA, Adams ME, Froehner SC, Agre P, Ottersen OP. 2003b. Delayed K^+ clearance associated with aquaporin-4 mislocalization: phenotypic defects in brains of alpha-syntrophin-null mice. Proc Natl Acad Sci USA. 100:13615–13620.

Ayata C, Lauritzen M. 2015. Spreading depression, spreading depolarizations, and the cerebral vasculature. Physiol Rev. 95:953–993.

Barlow JS. 1985. Methods of analysis of nonstationary EEGs, with emphasis on segmentation techniques: a comparative review. J Clin Neurophysiol. 2:267–304.

Basarsky TA, Duffy SN, Andrew RD, MacVicar BA. 1998. Imaging spreading depression and associated intracellular calcium waves in brain slices. J Neurosci. 18:7189–7199.

Binder DK, Yao X, Zador Z, Sick TJ, Verkman AS, Manley GT. 2006. Increased seizure duration and slowed potassium kinetics in mice lacking aquaporin-4 water channels. Glia. 53:631–636.

Chang JC, Shook LL, Biag J, Nguyen EN, Toga AW, Charles AC, Brennan KC. 2010. Biphasic direct current shift, haemoglobin desaturation and neurovascular uncoupling in cortical spreading depression. Brain. 133:996–1012.

Charles AC, Baca SM. 2013. Cortical spreading depression and migraine. Nat Rev Neurol. 9:637–644.

Chen TW, Wardill TJ, Sun Y, Pulver SR, Renninger SL, Baohan A, Schreiter ER, Kerr RA, Orger MB, Jayaraman V, et al. 2013. Ultrasensitive fluorescent proteins for imaging neuronal activity. Nature. 499:295–300.

Chuquet J, Hollender L, Nimchinsky EA. 2007. High-resolution in vivo imaging of the neurovascular unit during spreading depression. J Neurosci. 27:4036–4044.

Dana H, Mohar B, Sun Y, Narayan S, Gordus A, Hasseman JP, Tsegaye G, Holt GT, Hu A, Walpita D, et al. 2016. Sensitive red protein calcium indicators for imaging neural activity. Elife. 5:e12727.

Djukic B, Casper KB, Philpot BD, Chin LS, McCarthy KD. 2007. Conditional knock-out of Kir4.1 leads to glial membrane

depolarization, inhibition of potassium and glutamate uptake, and enhanced short-term synaptic potentiation. J Neurosci. 27:11354–11365.

Dreier JP, Reiffurth C. 2015. The stroke-migraine depolarization continuum. Neuron. 86:902–922.

Eilert-Olsen M, Haj-Yasein NN, Vindedal GF, Enger R, Gundersen GA, Hoddevik EH, Petersen PH, Haug FM, Skare O, Adams ME, et al. 2012. Deletion of aquaporin-4 changes the perivascular glial protein scaffold without disrupting the brain endothelial barrier. Glia. 60:432–440.

Enger R, Tang W, Vindedal GF, Jensen V, Johannes Helm P, Sprengel R, Looger LL, Nagelhus EA. 2015. Dynamics of ionic shifts in cortical spreading depression. Cereb Cortex. 25: 4469–4476.

Fenzl T, Romanowski CP, Flachskamm C, Honsberg K, Boll E, Hoehne A, Kimura M. 2007. Fully automated sleep deprivation in mice as a tool in sleep research. J Neurosci Methods. 166:229–235.

Haj-Yasein NN, Bugge CE, Jensen V, Ostby I, Ottersen OP, Hvalby O, Nagelhus EA. 2015. Deletion of aquaporin-4 increases extracellular K^+ concentration during synaptic stimulation in mouse hippocampus. Brain Struct Funct. 220: 2469–2474.

Haj-Yasein NN, Jensen V, Ostby I, Omholt SW, Voipio J, Kaila K, Ottersen OP, Hvalby O, Nagelhus EA. 2012. Aquaporin-4 regulates extracellular space volume dynamics during high-frequency synaptic stimulation: a gene deletion study in mouse hippocampus. Glia. 60:867–874.

Haj-Yasein NN, Jensen V, Vindedal GF, Gundersen GA, Klungland A, Ottersen OP, Hvalby O, Nagelhus EA. 2011. Evidence that compromised K^+ spatial buffering contributes to the epileptogenic effect of mutations in the human Kir4.1 gene (KCNJ10). Glia. 59:1635–1642.

Huber D, Gutnisky DA, Peron S, O'Connor DH, Wiegert JS, Tian L, Oertner TG, Looger LL, Svoboda K. 2012. Multiple dynamic representations in the motor cortex during sensorimotor learning. Nature. 484:473–478.

Kaifosh P, Zaremba JD, Danielson NB, Losonczy A. 2014. SIMA: Python software for analysis of dynamic fluorescence imaging data. In: Front Neuroinform. 8:80.

Koroleva VI, Bures J. 1993. Rats do not experience cortical or hippocampal spreading depression as aversive. Neurosci Lett. 149:153–156.

Kramer DR, Fujii T, Ohiorhenuan I, Liu CY. 2016. Cortical spreading depolarization: pathophysiology, implications, and future directions. J Clin Neurosci. 24:22–27.

Kudo C, Nozari A, Moskowitz MA, Ayata C. 2008. The impact of anesthetics and hyperoxia on cortical spreading depression. Exp Neurol. 212:201–206.

Leão AAP. 1944. Spreading depression of activity in the cerebral cortex. J Neurophysiol. 7:359–390.

Li X, Zima AV, Sheikh F, Blatter LA, Chen J. 2005. Endothelin-1-induced arrhythmogenic Ca^{2+} signaling is abolished in atrial myocytes of inositol-1,4,5-trisphosphate(IP3)-receptor type 2-deficient mice. Circ Res. 96:1274–1281.

Li YK, Wang F, Wang W, Luo Y, Wu PF, Xiao JL, Hu ZL, Jin Y, Hu G, Chen JG. 2012. Aquaporin-4 deficiency impairs synaptic plasticity and associative fear memory in the lateral amygdala: involvement of downregulation of glutamate transporter-1 expression. Neuropsychopharmacology. 37:1867–1878.

Lian XY, Stringer JL. 2004. Astrocytes contribute to regulation of extracellular calcium and potassium in the rat cerebral cortex during spreading depression. Brain Res. 1012:177–184.

Liu X, Gangoso E, Yi C, Jeanson T, Kandelman S, Mantz J, Giaume C. 2016. General anesthetics have differential inhibitory effects on gap junction channels and hemichannels in astrocytes and neurons. Glia. 64:524–536.

MacAulay N, Zeuthen T. 2012. Glial K^+ clearance and cell swelling: key roles for cotransporters and pumps. Neurochem Res. 37:2299–2309.

Malarkey EB, Ni Y, Parpura V. 2008. Ca^{2+} entry through TRPC1 channels contributes to intracellular Ca^{2+} dynamics and consequent glutamate release from rat astrocytes. Glia. 56: 821–835.

Marvin JS, Borghuis BG, Tian L, Cichon J, Harnett MT, Akerboom J, Gordus A, Renninger SL, Chen TW, Bargmann CI, et al. 2013. An optimized fluorescent probe for visualizing glutamate neurotransmission. Nat Methods. 10:162–170.

Minieri L, Pivonkova H, Harantova L, Anderova M, Ferroni S. 2015. Intracellular Na^+ inhibits volume-regulated anion channel in rat cortical astrocytes. J Neurochem. 132:286–300.

Mongin AA. 2016. Volume-regulated anion channel—a frenemy within the brain. Pflugers Arch. 468:421–441.

Nagelhus EA, Ottersen OP. 2013. Physiological roles of aquaporin-4 in brain. Physiol Rev. 93:1543–1562.

Orser BA, Canning KJ, Macdonald JF. 2002. Mechanisms of general anesthesia. Curr Opin Anesthesiol. 15:427–433.

Padmawar P, Yao X, Bloch O, Manley GT, Verkman AS. 2005. K^+ waves in brain cortex visualized using a long-wavelength K^+-sensing fluorescent indicator. Nat Methods. 2:825–827.

Peters O, Schipke CG, Hashimoto Y, Kettenmann H. 2003. Different mechanisms promote astrocyte Ca^{2+} waves and spreading depression in the mouse neocortex. J Neurosci. 23:9888–9896.

Pietrobon D, Moskowitz MA. 2014. Chaos and commotion in the wake of cortical spreading depression and spreading depolarizations. Nat Rev Neurosci. 15:379–393.

Saadoun S, Tait MJ, Reza A, Davies DC, Bell BA, Verkman AS, Papadopoulos MC. 2009. AQP4 gene deletion in mice does not alter blood-brain barrier integrity or brain morphology. Neuroscience. 161:764–772.

Seidel JL, Escartin C, Ayata C, Bonvento G, Shuttleworth CW. 2016. Multifaceted roles for astrocytes in spreading depolarization: A target for limiting spreading depolarization in acute brain injury? Glia. 64:5–20.

Shigetomi E, Patel S, Khakh BS. 2016. Probing the complexities of astrocyte calcium signaling. Trends Cell Biol. 26:300–312.

Smith RH, Levy JR, Kotin RM. 2009. A simplified baculovirus-AAV expression vector system coupled with one-step affinity purification yields high-titer rAAV stocks from insect cells. Mol Ther. 17:1888–1896.

Sonn J, Mayevsky A. 2006. Effects of anesthesia on the responses to cortical spreading depression in the rat brain in vivo. Neurol Res. 28:206–219.

Srinivasan R, Huang BS, Venugopal S, Johnston AD, Chai H, Zeng H, Golshani P, Khakh BS. 2015. Ca^{2+} signaling in astrocytes from $Ip3r2^{-/-}$ mice in brain slices and during startle responses in vivo. Nat Neurosci. 18:708–717.

Takano T, Tian GF, Peng W, Lou N, Libionka W, Han X, Nedergaard M. 2006. Astrocyte-mediated control of cerebral blood flow. Nat Neurosci. 9:260–267.

Tang W, Ehrlich I, Wolff SB, Michalski AM, Wolfl S, Hasan MT, Luthi A, Sprengel R. 2009. Faithful expression of multiple proteins via 2A-peptide self-processing: a versatile and reliable method for manipulating brain circuits. J Neurosci. 29: 8621–8629.

Thrane AS, Rangroo Thrane V, Zeppenfeld D, Lou N, Xu Q, Nagelhus EA, Nedergaard M. 2012. General anesthesia selectively disrupts astrocyte calcium signaling in the awake mouse cortex. P Natl Acad Sci USA. 109: 18974–18979.

Thrane AS, Rappold PM, Fujita T, Torres A, Bekar LK, Takano T, Peng W, Wang F, Rangroo Thrane V, Enger R, et al. 2011. Critical role of aquaporin-4 (AQP4) in astrocytic Ca^{2+} signaling events elicited by cerebral edema. P Natl Acad Sci USA. 108:846–851.

Thrane AS, Takano T, Rangroo Thrane V, Wang F, Peng W, Ottersen OP, Nedergaard M, Nagelhus EA. 2013. In vivo NADH fluorescence imaging indicates effect of aquaporin-4 deletion on oxygen microdistribution in cortical spreading depression. J Cerebr Blood Flow Metab. 33:996–999.

Tran CH, Gordon GR. 2015. Astrocyte and microvascular imaging in awake animals using two-photon microscopy. Microcirculation. 22:219–227.

Verkman AS, Anderson MO, Papadopoulos MC. 2014. Aquaporins: important but elusive drug targets. Nat Rev Drug Discov. 13:259–277.

Xie L, Kang H, Xu Q, Chen MJ, Liao Y, Thiyagarajan M, O'Donnell J, Christensen DJ, Nicholson C, Iliff JJ, et al. 2013. Sleep drives metabolite clearance from the adult brain. Science. 342:373–377.

Yao X, Hrabetova S, Nicholson C, Manley GT. 2008. Aquaporin-4-deficient mice have increased extracellular space without tortuosity change. J Neurosci. 28:5460–5464.

Zhang H, Verkman AS. 2008. Aquaporin-4 independent Kir4.1K^+ channel function in brain glial cells. Mol Cell Neurosci. 37: 1–10.